Fast 3-D Electromagnetic Full-Wave Inversion of Dielectric Anisotropic Objects Based on ResU-Net Enhanced by Variational Born Iterative Method

Junjie Fei, Yanjin Chen, Miao Zhong, and Feng Han, *Senior Member, IEEE*

***Abstract*— In this article, a novel artificial neural network named residual U-Net (ResU-Net) is proposed to directly reconstruct 3-D dielectric anisotropic objects from scattered electromagnetic field data recorded at the receiver array. ResU-Net has the same framework as that of U-Net but the convolution kernels are replaced with residual kernels. Meanwhile, the squeeze-and-excitation (SE) operation is added to enable information interaction among different channels and further improve prediction accuracy. ResU-Net is trained by thousands of 3-D homogeneous dielectric anisotropic handwritten digits and the corresponding synthesized scattered field data. In the online prediction, ResU-Net can invert multiple anisotropic model parameters of homogeneous 3-D objects instantaneously. For an inhomogeneous object or multiple homogeneous objects, ResU-Net provides good initial profiles which are fed into the following variational Born iterative method (VBIM) full-wave inversion solver. In addition, the VBIM is implemented in a restricted domain instead of the whole 3-D inversion domain to save computational cost. Numerical experiments show that compared with the traditional iterative solver, such as VBIM, the proposed ResU-Net or the hybrid method can not only achieve higher reconstruction accuracy but also accomplish the multiparametric 3-D inversion in a much faster way.**

***Index Terms*— Dielectric anisotropic objects, electromagnetic (EM) full-wave inversion (FWI), residual network, U-Net, variational Born iterative method (VBIM).**

I. Introduction

ELECTROMAGNETIC (EM) full-wave inversion (FWI) is a strict whole wavefield matching procedure that aims at obtaining quantitative information of the unknown objects by minimizing the mismatch function between simulated and measured field data. Compared with the qualitative EM imaging methods, FWI can quantitatively reconstruct multiple model parameters of unknown objects and has the advantage of high resolution.

The development of EM FWI can date the back to early eighties of the last century. In the beginning, due to the limitation of computer ability, only one 1-D constitutive parameter of an inhomogeneous scatterer was reconstructed by iterative methods [1]. Later, the research work was extended to the simultaneous reconstruction of both permittivity and conductivity of 1-D profiles by Habashy *et al.* [2]. Wang and Chew proposed the Born iterative method (BIM) to solve the 2-D electromagnetic nonlinear inverse scattering problem [3]. They then also proposed the distorted BIM (DBIM) to reconstruct 2-D scatterer profiles [4] by simultaneously updating their dielectric parameters and Green's functions in each iteration. BIM has another variant variational BIM (VBIM) [5] which updates the perturbations of scatterer model parameters instead of the parameters themselves. Therefore, VBIM has higher inversion accuracy than BIM due to the tiny adjustments of the model parameters in each iteration. Besides the Born-type iterative methods, there are other FWI methods, such as the contrast source inversion (CSI) and the subspace-based optimization method (SOM), which have been widely applied to the 2-D inversion. CSI is different from BIM since it has no forward computation. Its cost function is constructed using the summation of mismatches of the contrasts and contrast sources [6]. In the areas of through-wall imaging [7] and biomedical imaging [8], CSI has been successfully put into effect. The subspace optimization method (SOM) is similar to CSI. However, its FWI iteration is implemented in the subspace of the induced current. Details can be found in [9]. It has been combined with the frequency hopping technique and used to invert for 2-D anisotropic dielectric objects with large electrical dimensions [10], [11]. Another noteworthy FWI development branch in the past decades is the hybrid method. For example, Ye *et al.* [12] proposed the SOM-DBIM to achieve super-resolution images of 2-D biaxial anisotropic objects under the illumination of the transverse electric (TE) wave. In [13], the DBIM and BIM were combined to guarantee both the convergence speed and solution resolution. In addition, both the aforementioned independent and hybrid methods also have been applied to 3-D inversion. See the Born-type methods for the reconstruction of 3-D isotropic objects [14]–[16] or anisotropic objects [17]–[20], inversion of airborne electromagnetic data [21], [22], and imaging of human tissues [23]–[25], and the applications of CSI and SOM-DBIM for 3-D FWI [26]–[28].

However, these iterative methods have the defect of high computational cost, which is especially obvious for the reconstruction of 3-D arbitrary anisotropic objects [29]. Fortunately, thanks to the appearance and fast evolution of machine

Manuscript received 19 August 2021; revised 8 November 2021; accepted 13 December 2021. Date of publication 5 January 2022; date of current version 8 September 2022. *(Corresponding author: Feng Han.)*

The authors are with the Key Laboratory of Electromagnetic Wave Science and Detection Technology, Institute of Electromagnetics and Acoustics, Xiamen University, Xiamen 361005, China (e-mail: feng.han@xmu.edu.cn).

Color versions of one or more figures in this article are available at https://doi.org/10.1109/TAP.2021.3138551.

Digital Object Identifier 10.1109/TAP.2021.3138551

0018-926X © 2022 IEEE. Personal use is permitted, but republication/redistribution requires IEEE permission.
See https://www.ieee.org/publications/rights/index.html for more information.

learning (ML), EM FWI based on the artificial neural network (ANN) can retrieve the scatterer model parameters in a real-time fashion. Its development almost follows the same line of traditional FWI, i.e., from low dimension to high dimension and from a single-parameter inversion to pixel-based inversion. Originally, the ANN is only employed to extract rather general information about the geometric and dielectric properties of the scatterers, such as their positions, sizes, shapes, and piecewise constant permittivities [30], [31]. Later, researchers proposed several 2-D pixel-based inversion methods based on ANNs to account for spatially inhomogeneous scatterers or multiple scatterers in the inversion domain. These methods can be roughly categorized into four kinds [32], the direct learning approach, the physics-assisted learning approach, the learning-assisted objective-function approach, and other approaches. In direct learning, the measured scattered field data are directly converted into the scatterer model parameters. The ANN directly learns their nonlinear relationship. Representative research works have been presented in [33]–[35]. It has the drawback that the input and output of the ANN have different data types. Therefore, the ANN must learn the underlying wave physics of EM scattering. The physics-assisted learning approach overcomes this defect by first converting EM field data into preliminary dielectric images of the scatterers using approximate but fast inverse solvers, e.g., Born approximation (BA) or backpropagation (BP), and then training the ANN using the obtained preliminary model parameters and true scatterer parameters. As a consequence, the input and output of the ANN have the same data type. A series of related research results have been given in [33] and [36]–[39]. The learning-assisted objective-function approach also combines the ANN and the traditional inversion solver. Nevertheless, the output of the ANN feeds the iterative inversion solver, which further refines the scatterer model parameters [40]–[42]. Besides these three types of ANN inversion methods, there are also other means to apply ANN in EM FWI [43]. Recently, ANNs are also used for 3-D FWI. For example, in [44], inhomogeneous 3-D objects embedded inside layered media are reconstructed by the physics-assisted learning approach. In [45], the super-resolution images of multiple 3-D objects are directly reconstructed from the measured scattered field data by an extreme learning machine. However, all these works regarding 3-D inversion by ANNs are only for isotropic objects.

In this article, for the first time, we achieve the direct reconstruction of 3-D objects with dielectric arbitrary anisotropy by a residual U-Net (ResU-Net). Its overall architecture is similar to U-Net [46]. However, it incorporates residual learning blocks to account for the gradient vanishing and exploding problems in deep learning [47]. In addition, a squeeze-and-excitation (SE) operation [48] is embedded inside ResU-Net to enable information interaction among different channels and further improve its prediction accuracy. The details of the proposed ResU-Net can be found in Section II-B. Moreover, for homogeneous anisotropic scatterers, the ResU-Net is trained in the direct learning mode and reconstructs their dielectric profiles instantaneously. However, for inhomogeneous anisotropic scatterers or multiple homogeneous anisotropic scatterers, the VBIM solver is connected to ResU-Net to highlight the inhomogeneity. In other words, the ANN inversion follows the method of learning-assisted objective function.

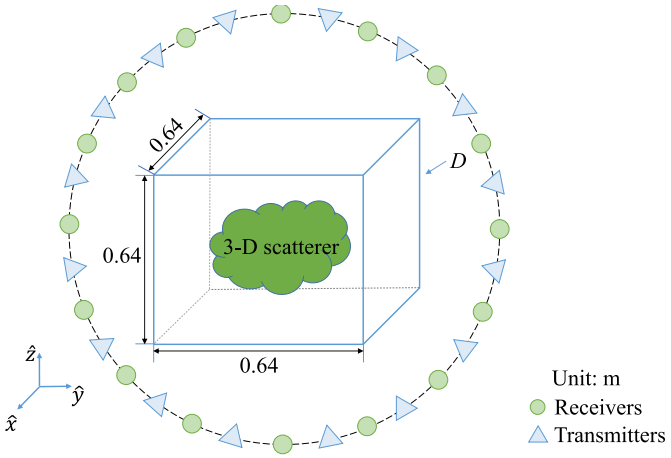

Fig. 1. 3-D FWI model configuration. There are N_t transmitters and N_r receivers placed around the inversion domain D.

The rest of this article is organized as follows. In Section II, the conventional VBIM and the ResU-Net are described in detail. In Section III, two numerical examples are used to verify the proposed method. The first one is for homogeneous dielectric anisotropic scatterers. The second one is for inhomogeneous and multiple homogeneous dielectric anisotropic scatterers. Finally, in Section IV, the summary, conclusion, and future work are presented.

II. Methods

In this section, first, the traditional FWI based on VBIM is briefly introduced. Then, the configuration of the ResU-Net is given in detail. Finally, the hybridization of ResU-Net and VBIM for the inversion of inhomogeneous anisotropic scatterers is also given.

A. VBIM

Suppose the nonmagnetic dielectric arbitrary anisotropic scatterers are embedded in the free space and transmitters and receivers are placed surrounding them, as shown in Fig. 1. The forward scattering is described by the state equation [19]

$$\mathbf{E}_{inc}(\mathbf{r}) = \mathbf{E}_{tot}(\mathbf{r}) - \mathbf{E}_{sct}(\mathbf{r}) = \overline{\overline{\epsilon}}^{-1}(\mathbf{r})\frac{\mathbf{D}_{tot}(\mathbf{r})}{\varepsilon_0} - j\omega\int_D \overline{\overline{\mathbf{G}}}_{\mathbf{EJ}}(\mathbf{r},\mathbf{r}')\cdot\overline{\overline{\chi}}(\mathbf{r}')\mathbf{D}_{tot}(\mathbf{r}')d\mathbf{r}' \quad (1)$$

where $\overline{\overline{\mathbf{G}}}_{\mathbf{EJ}}$ is the dyadic Green's function in the homogeneous free space [49] and D is the inversion domain enclosing the scatterers. The contrast function $\overline{\overline{\chi}}$ is defined as

$$\overline{\overline{\chi}}(\mathbf{r}) = [\overline{\overline{\epsilon}}(\mathbf{r}) - \overline{\overline{\mathbf{I}}}]\overline{\overline{\epsilon}}^{-1}(\mathbf{r}) \quad (2)$$

where $\overline{\overline{\epsilon}}$ is the complex relative permittivity tensor. It is computed by

$$\overline{\overline{\epsilon}} = \begin{bmatrix} \varepsilon_{11} & \varepsilon_{12} & \varepsilon_{13} \\ \varepsilon_{21} & \varepsilon_{22} & \varepsilon_{23} \\ \varepsilon_{31} & \varepsilon_{32} & \varepsilon_{33} \end{bmatrix} + \frac{1}{j\omega\varepsilon_0}\begin{bmatrix} \sigma_{11} & \sigma_{12} & \sigma_{13} \\ \sigma_{21} & \sigma_{22} & \sigma_{23} \\ \sigma_{31} & \sigma_{32} & \sigma_{33} \end{bmatrix} \quad (3)$$

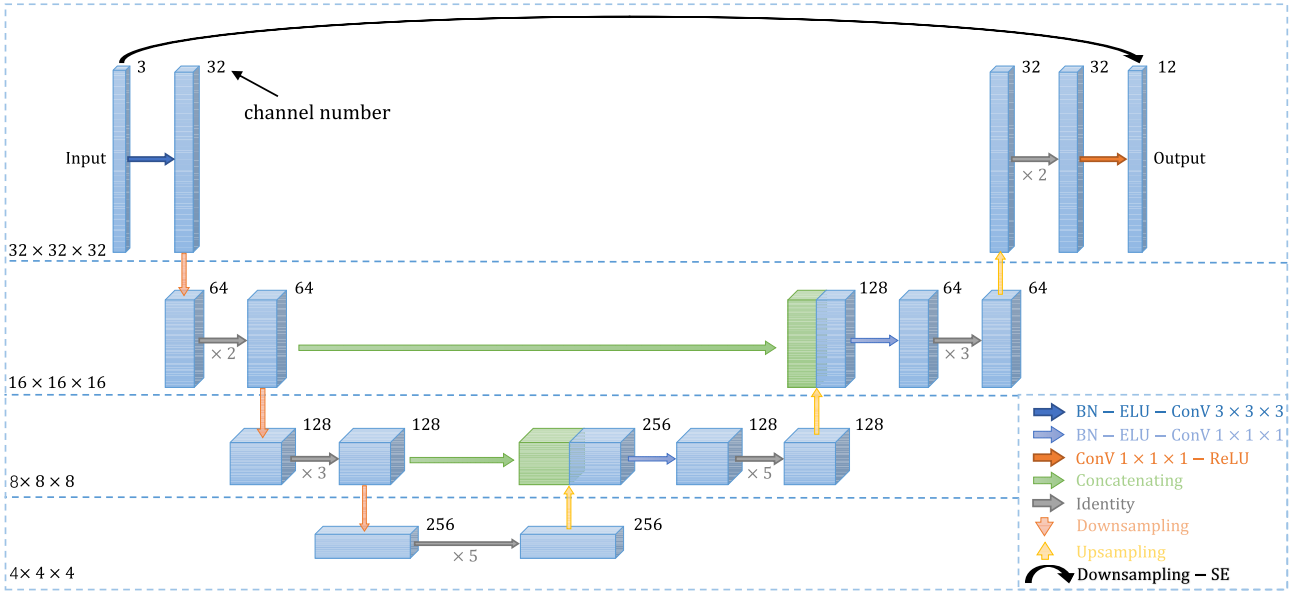

Fig. 2. Architecture of the ResU-Net.

where $\varepsilon_{pq} = \varepsilon_{qp}$ and $\sigma_{pq} = \sigma_{qp}$ with $p, q = 1, 2$ and 3. In other words, we only consider the symmetrical tensors which are ubiquitous in nature [50]. In the forward scattering computation, (1) is discretized and $\mathbf{D}_{tot}$ is expanded by the rooftop basis functions. The coefficients are solved by the stabilized biconjugate-gradient fast Fourier transform (BCGS-FFT). Details can be found in [19] and will not be repeated here.

The inverse scattering is formulated by the data equation which is expressed as [19]

$$\mathbf{E}_{sct}(\mathbf{r}) = j\omega \int_D \overline{\overline{\mathbf{G}}}_{\mathbf{EJ}}(\mathbf{r}, \mathbf{r}') \cdot \overline{\overline{\chi}}(\mathbf{r}') \mathbf{D}_{tot}(\mathbf{r}') d\mathbf{r}' \tag{4}$$

where $\mathbf{E}_{sct}$ is the scattered EM field measured at the receiver array. In the inverse computation, (4) is discretized and we obtain a matrix-form equation in which the sensitivity matrix is composed by the total field $\mathbf{E}_{tot}$ and the DGFs [19]. The unknown contrast $\overline{\overline{\chi}}$ is solved by the conjugate gradient (CG) method. One should note that $\mathbf{E}_{tot}$ also depends on $\overline{\overline{\chi}}$. Therefore, (4) is nonlinear. In VBIM, it is linearized by replacing $\mathbf{E}_{tot}$ in the current iteration with that obtained by BCGS-FFT in the last iteration. For the detailed procedure of VBIM, see [19, Sec. II]. In addition, the results in [19] also show that the convention VBIM is rather time consuming, which is especially obvious for the inversion of 3-D arbitrary anisotropic objects.

B. ResU-Net

As mentioned in Section I, we combine U-Net and residual networks to account for both the voxel-level reconstruction and deep learning demands. The overall architecture of this ResU-Net is shown in Fig. 2. It has the U-Net framework and is realized in four levels. However, its major difference with respect to U-Net is that the convolution operations in U-Net are replaced by residual operations, which are shown in Fig. 3. The dimensions of data blocks in each level of ResU-Net are stamped in the lower left corner and their channel numbers are marked near the block. The data blocks in two different levels are connected by the downsampling or upsampling operation, depending on the left branch (encoder) or the right branch (decoder). The encoder is used for feature extraction and the decoder restores the high-level semantic features in order to build a mapping from the scattered EM fields to the model parameters of unknown scatterers for the voxel-level prediction. The input of the encoder with three channels is preprocessed by a series of operations, including the batch-normalization (BN), the activation function ELU and a $3 \times 3 \times 3$ convolutional (ConV) kernel. Then, the data block with 32 channels is manipulated by three rounds of downsampling-identity $\times n$ to extract the main features of the scatterer parameters. Identity $\times n$ means identity operation cascaded n times. In the decoder, the network structure is similar to that in the encoder. However, upsampling is adopted to restore the 3-D dielectric parameter images. Another notable operation in the decoder is the concatenation which is used to directly integrate features extracted in the encoder to the decoder. The purpose of such an operation is to avoid feature loss in the deep learning process. Following the concatenated data blocks are a series of BN-ELU-ConV with the kernel size of $1 \times 1 \times 1$ which is used to guarantee the data block dimension consistency. As shown in Fig. 2, the concatenating operation in the first level is different from those in the second and third levels since it includes a series of downsampling operations and its overall structure is similar to an SE operation. See Fig. 3(d). Finally, in front of the output data block, a convolution kernel with the size of $1 \times 1 \times 1$ followed by the ReLU activation function is used to generate 12 nonnegative dielectric model parameters (six for permittivity tensor and six for conductivity tensor).

The residual operations in the proposed architecture are manifested by modified identity, downsampling, and upsampling, as shown in Fig. 3. For all three operations, each

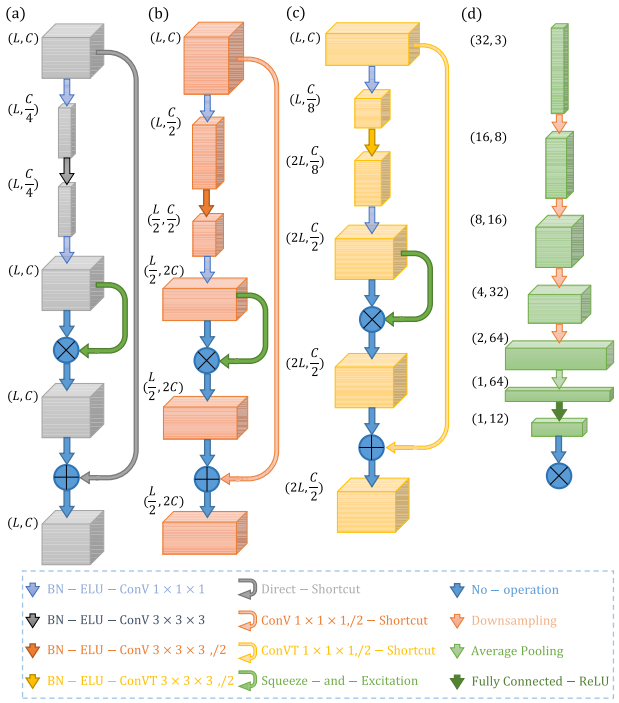

Fig. 3. Detailed residual operations for (a) identity, (b) downsampling, (c) upsampling, and (d) downsampling-SE in Fig. 2. (L, C) means the data block has the dimensions of $L \times L \times L$ and the channel number is C. (32, 3) means the data block has the dimensions of $32 \times 32 \times 32$ and the channel number is 3.

includes three basic parts. The first part is a "bottleneck" which is composed of three successive convolutions that are used to reduce the number of parameters and increase ANN depth. In addition, the pre-activation strategy, including BN and ELU is adopted before the convolution layer inside the "bottleneck," which has been shown by several numerical experiments having more accurate prediction than other activation strategies [51]. Here, we use the activation function ELU instead of ReLU since the ResU-Net maps the scattered field data to scatterer dielectric parameters. The intermediate variables may have negative values except those in the outermost output layer. The major differences among the three operations of identity, downsampling, and upsampling lie in the stride sizes and channel sizes of the BN-ELU-Conv. The first and the third convolutions in all three operations have the same stride size 1. However, for the second convolution, its stride size is 1 for the identity but 2 for both upsampling and downsampling. But note the convolution in the upsampling is actually the transposed convolution (T-Conv) instead of the regular convolution. In addition, the channel numbers of three convolutions of the "bottleneck" in three operations are also set different values to accommodate the data block size consistency in the whole ResU-Net. The second part is the SE operation which includes a series of operations of global pooling (GP)-FC-ReLU-FC-Sigmoid. Its results are multiplied with the output of the first part and the purpose of such an operation is to increase the information fusion among different channels and further improve the prediction accuracy of the whole ANN [48]. The third part is an adding operation that realizes the residual computation between the input of the "bottleneck" and the output of the SE operation. Again, the residual operation is adopted to increase the ANN depth to accommodate the nonlinearity and ill-posedness of the 3-D FWI of anisotropic scatterers. In addition, the shortcuts for the adding operations for identity, downsampling, and upsampling are also different due to the different output data block sizes of the SE operations.

Fig. 3(d) shows the major procedure of the downsampling-SE which directly bridges the input and output of the ResU-Net. Several consecutive downsampling operations are implemented to reduce the data block size to $1 \times 1 \times 1$ and increase the channel number to 64. Then, the global average pooling and the FC-ReLU are taken to reduce the channel number to 12 and map the scattered field data to 12 dielectric arbitrary anisotropic model parameters. They are then directly multiplied to the U-Net output. The purpose of downsampling-SE is to strengthen the direct inversion of values of homogeneous model parameters and prevent their information loss in the deep U-Net.

For 3-D EM inversion by ResU-Net, we choose the mean square error (MSE) [52] between the ground truths and the predicated model parameters as the loss function for training. It is defined as

$$MSE = \frac{1}{N}\sum_{n=1}^{N} \|\hat{\mathbf{y}}_n - \mathbf{y}_n\|_2^2 \tag{5}$$

where $\mathbf{y}_n$ and $\hat{\mathbf{y}}_n$ are the ground truth vector and the predicted model parameter vector in the nth voxel, respectively. Both of them have the dimension of 12×1 and contain 12 dielectric parameters. $\|\|_2$ denotes the L_2 norm and N is the total number of voxels in the inversion domain. The parameters of the 3-D ResU-Net will be adjusted in each training epoch. The optimization method used in this work is the Adam optimizer [53]. Because partial data are used to validate the ResU-Net after training, the MSE defined in (5) is also suitable for a validation error.

C. Hybridization of ResU-Net And VBIM

Due to the strong nonlinearity and ill-posedness of EM inversion for dielectric arbitrary anisotropic scatterers, the proposed ResU-Net cannot completely and precisely reconstruct inhomogeneous or multiple homogeneous objects in the voxel level. Therefore, we cascade the ResU-Net and the conventional VBIM solver. In other words, the VBIM solver treats the ResU-Net output as the initial profiles of the 3-D objects and implements the iteration to further improve the reconstruction accuracy. Another important point deserving emphasizing here is that VBIM is implemented in a restricted region instead of the whole inversion domain. When we obtain the preliminary inversion results by ResU-Net, the background region is clearly discernible although model parameters in the scatterer voxels may be inaccurate. Therefore, we downsize the inversion domain by removing the peripheral "background" voxels that are two voxels away from the preliminary scatterers. Here, "removing" means the background model parameters in these voxels are known and will not be inverted. As a

consequence, the computational cost of VBIM is significantly reduced. And this will be shown in Section III-C.

III. Numerical Results

In this section, we first briefly introduce the training details of the proposed ResU-Net and validate its design superiority by several comparative numerical analyses. Then, two numerical examples are given to verify the feasibility and effectiveness of ResU-Net for the inversion of 3-D dielectric anisotropic objects. In the first example, 12 dielectric parameters of the homogeneous scatterer are directly reconstructed from scattered EM field data. The ResU-Net realizes the instantaneous multiparametric inversion of anisotropic objects. In the second example, the hybrid solver of ResU-Net and VBIM is used to reconstruct an inhomogeneous scatterer or multiple homogeneous scatterers from scattered field data contaminated by noise. The inversion results and computational cost are compared with those by the pure VBIM solver. The purpose of this example is to show the practicality of the hybrid method for the inversion of inhomogeneous dielectric arbitrary anisotropic objects. In addition, in order to quantitatively evaluate the reconstruction performance of the proposed method, we use the data misfit and model misfit defined in [54, Eqs. (16) and (17)]. The data misfit indicates how well the measured scattered fields match the predicted scattered fields in the iterations. The model misfit indicates how well the reconstructed model parameters match the true model parameters. It represents the relative error between the ground truth and the numerical inversion result. All the measured scattered EM field data are simulated by the BCGS-FFT forward solver. All the numerical experiments are performed on a workstation with an 18-cores Intel i9-10980XE 3.00 GHz CPU and 256 GB RAM. The ResU-Net is trained on an NVIDIA GeForce RTX 3090 GPU with 24 GB memory.

A. EM Inversion Setups and ResU-Net Training Details

As shown in Fig. 1, the inversion domain D has the size of 0.64 m $\times$ 0.64 m $\times$ 0.64 m with its center locating at the origin of the coordinate. It is discretized into 32 $\times$ 32 $\times$ 32 voxels in the FWI. Because there are 12 anisotropic parameters to be reconstructed in each voxel, the output data block of ResU-Net has the dimensions of 32 $\times$ 32 $\times$ 32 and 12 channels. Totally, 32 transmitters and 32 receivers are placed in two concentric spheres with radii of 1 and 2 m, respectively. The transmitters are arranged in four circles with their faces parallel to the sphere equatorial plane. In each circle, eight transmitters are uniformly placed with an equal arc interval. The latitudes of four circles are 18°N, 54°N, 18°S, and 54°S, respectively. The receivers are arranged in a similar way. Note the transmitters are assumed to be infinitesimal dipoles and their radiation pattern is accounted for by Green's functions. In the inversion, we use 16 operation frequencies from 160 to 460 MHz with an equal interval of 20 MHz which are the same as those used in the forward computation to generate the training samples. Because the scattered electric fields are complex numbers and have three orthogonal components, the input data block of ResU-Net has the dimensions of 32 $\times$ 32 $\times$ 32 and three channels. The first dimension is corresponding to 32 transmitters. The second dimension is corresponding to 32 receivers. The third dimension is for the combination of 16 frequencies and the real and imaginary parts of the data. The three channels are corresponding to three orthogonal scattered electrical field components, respectively.

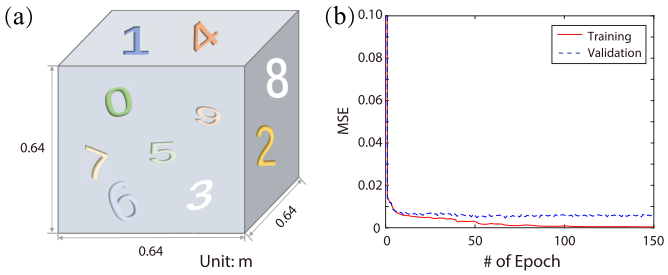

Fig. 4. (a) Training and validation models of ResU-Net. (b) Convergence curves of training and validation.

TABLE I
Comparisons of the Proposed ResU-Net and Those Designs Achieved by Replacing Its Certain Components

	ResU-Net	post-activation	SE removed	three levels	five levels
MSE	0.004784	0.005788	0.005478	0.005676	0.004884
NNP	1,757,176	1,756,652	1,440,220	320,312	4,799,160

Remark: NNP means number of network parameters.

As shown in Fig. 4(a), the training dataset is constructed by ten basic 3-D numerals adapted from the MNIST [55] which is originally used in the field of 2-D ML. We stretch the numerals in the perpendicular direction and rotate them by 90°, 180°, or 270°, respectively, to enrich the database. For each training sample, only one numeral appears in the inversion domain. Although its location is random, the values of the diagonal elements of $\overline{\overline{\varepsilon}}_r$ are randomly set in the range of [1.2, 2.0] and those of the nondiagonal elements distribute between 0.1 and 0.5. The conductivity elements are assigned random values between 1 and 5 mS/m. It should be pointed out that the 3-D digit of each training sample is homogeneous. The inversion inaccuracy for inhomogeneous objects caused by the trained ResU-Net is compensated by the VBIM solver, which will be discussed in Section III-C. Using the above strategy, 3000 samples are randomly generated for training and 100 are for validation. After 150 epochs of training on the RTX 3090 GPU which costs about 50 min, the training MSE decreases to less than 0.0004 and the validation MSE becomes less than 0.00457. Add both of them almost keep unchanged after the 100th epoch, as shown in Fig. 4(b). In other words, the ResU-Net is fully trained and ready for 3-D dielectric arbitrary anisotropic FWI.

We then validate the superiority of the design of our ResU-Net by replacing its certain component with the conventional design and comparing the number of network parameters and final training MSE. Note this final MSE is obtained by repeating the training five times with random initial values of the network parameters and taking the mean value of five MSEs. Four numerical experiments are conducted. In the

TABLE II
MODEL MISFITS OF THE RECONSTRUCTED ANISOTROPIC DIELECTRIC PARAMETERS BY RESU-NET IN TEST #1 AND TEST #2

Parameters	ϵ_{11}	ϵ_{22}	ϵ_{33}	ϵ_{12}	ϵ_{13}	ϵ_{23}	σ_{11}	σ_{22}	σ_{33}	σ_{12}	σ_{13}	σ_{23}
Test #1	0.02953	0.03374	0.04117	0.48505	0.49772	0.48970	0.48361	0.48869	0.48370	0.48869	0.48263	0.48455
Test #2	0.03824	0.04959	0.05326	0.54493	0.56454	0.55633	0.54528	0.63617	0.54329	0.63617	0.58584	0.54926

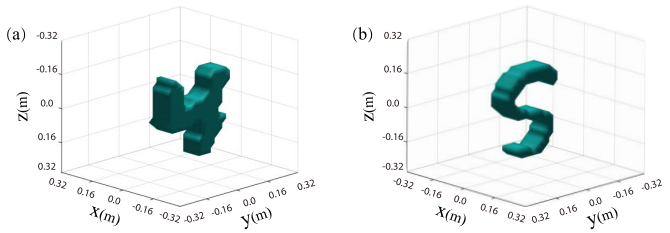

Fig. 5. 3-D shapes of the objects in (a) Test #1 and (b) Test #2.

first experiment, the pre-activation of BN-ELU in the three operations including identity, downsampling, and upsampling (see Fig. 3) is replaced by the conventional postactivation. In the second experiment, the SEs in all three operations are removed. In the third and fourth experiments, the overall architecture of the ResU-Net is modified having three or five levels. Table I shows comparisons of MSE values and the number of network parameters. We can see that MSE increases from 0.004784 to 0.005788 if the pre-activation strategy is replaced by the postactivation strategy although the number of network parameters has no obvious change. If we remove the SEs in the three operations, the MSE increases more than 21%, which will without question lead to the degeneration of the ResU-Net inversion performance. For the comparisons for network levels, it is obvious that the ResU-Net significantly deteriorates if we only use three levels although the network parameters are also significantly reduced. However, if we keep increasing the level number, i.e., increasing the network depth, its performance actually has no obvious improvement. However, its capacity becomes much larger. All those comparisons indicate the current design of the ResU-Net is the most appropriate.

B. Case 1: Single Homogeneous Anisotropic Scatterer

In this case, we implement two tests to validate the performance of the proposed ResU-Net. In both tests, the objects are homogeneous and their 3-D shapes are shown in Fig. 5. The object in Test #1 is the homogeneous digit "4." Although its basic shape is similar to those of training samples, its thickness, location, and 12 anisotropic dielectric parameters are distinct. For convenience, we only select the 2-D xy cross section and show the results in Fig. 6. In Test #2, we use ResU-Net to reconstruct the 3-D homogeneous anisotropic letter "S" whose shape and parameters are far from those in the training dataset. Similarly, the xy cross sections of the inversion results are shown in Fig. 7. The model misfits of the reconstructed dielectric parameters in both tests are listed in Table II. One should note that Test #1 is used to validate the inversion performance of the proposed ResU-Net, while Test #2 is used to validate its generalization ability.

By combining the graphical results shown in Figs. 6 and 7 and the model misfit values listed in Table II, we made the following three observations: 1) the prediction of the diagonal elements of the relative permittivity tensor is obviously more accurate than that of the nondiagonal elements and all the elements in the conductivity tensor. This is manifested by both the reconstructed dielectric profiles and model misfit values. The different prediction accuracy is due to the fact that the diagonal elements of the relative permittivity tensor are larger than the nondiagonal elements and the conductivity values. As a result, the trained ResU-Net is more sensitive to the diagonal elements of the relative permittivity tensor in the full-wave inversion. In addition, one should note that there is another significant reason which leads to the large model misfits of the nondiagonal elements of the relative permittivity tensor and conductivity values in all anisotropic tensor elements. Their values of the background medium are zero. Therefore, the denominators in the model misfit computation are rather small (see (16) in [54]), which causes large model misfit values. 2) The prediction accuracy in Test #2 is lower than that in Test #1. This can be easily observed by comparing the similarities of the reconstructed dielectric profiles and ground truths in Figs. 6 and 7 and the model misfit discrepancies listed in Table II. Such a different inversion accuracy is expected. The digit "4" is similar to the training samples. The letter "S" is out of the range of the training dataset. The trained ResU-Net is more adaptive to the 3-D object similar to the training samples. 3) The mean model misfit of the diagonal elements of the relative permittivity tensor is 3.48% for the digit "4" and 4.7% for the letter "S." The proposed ResU-Net has good multiple parameter inversion accuracies and generalization ability for a single 3-D homogeneous dielectric arbitrary anisotropic object. This is also proved by the inverted multiple dielectric parameters shown in Figs. 6 and 7.

C. Case 2: Single Inhomogeneous Anisotropic Scatterer or Multiple Homogeneous Anisotropic Scatterers

We then test the trained ResU-Net using an inhomogeneous anisotropic object and multiple homogeneous anisotropic objects although they never show up in the training dataset. In Test #3, the 3-D object is the inhomogeneous letter "C" and there are two homogeneous cuboids presented in the inversion domain in Test #4. Their 3-D shapes are shown in Fig. 8.

For Test #3, the ground truths of the object dielectric profiles and the reconstructed permittivity and conductivity profiles by ResU-Net are shown in the first and second columns of Figs. 9 and 10, respectively. We can see that the ResU-Net can only recover the object shape. It fails to invert the

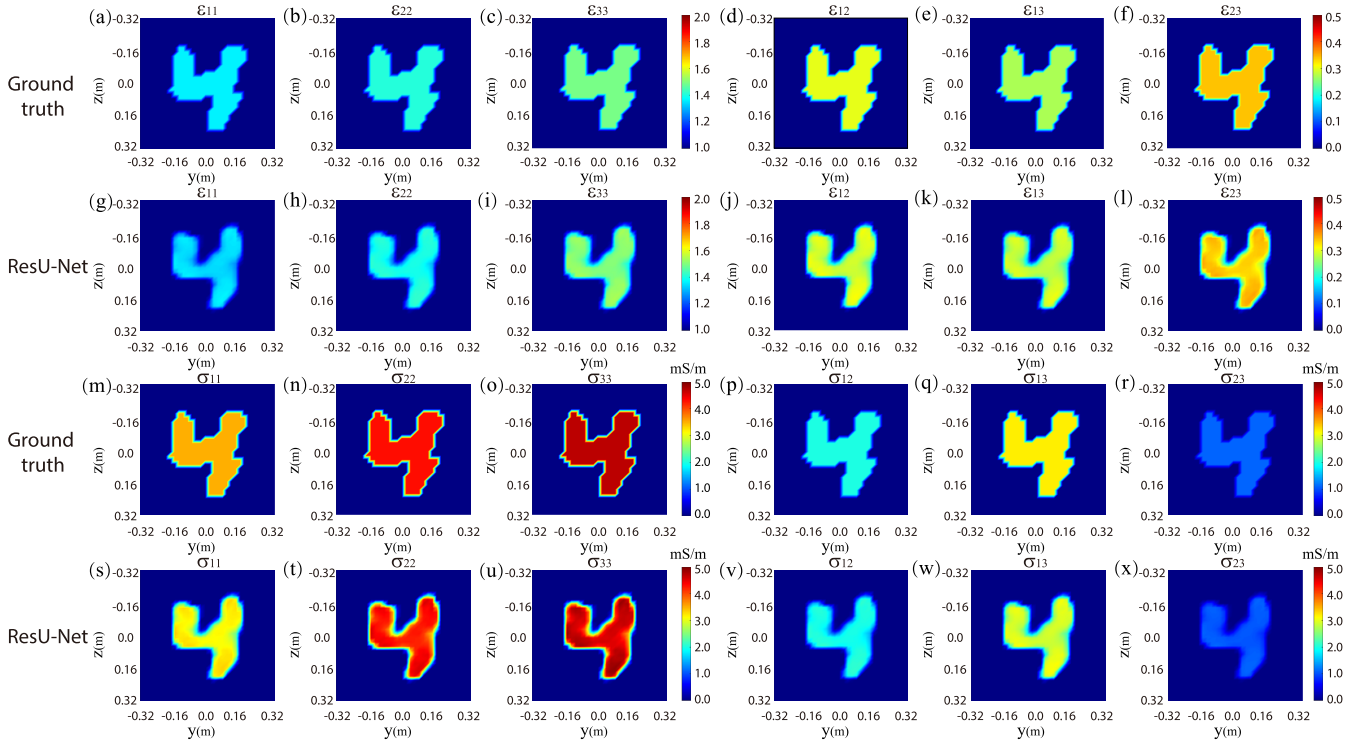

Fig. 6. Test #1: the inversion results of the homogeneous digital "4" by ResU-Net and the ground truths. The first and the third rows display the ground truths of anisotropic permittivity and conductivity. The second and the fourth rows display the reconstructed anisotropic profiles of permittivity and conductivity.

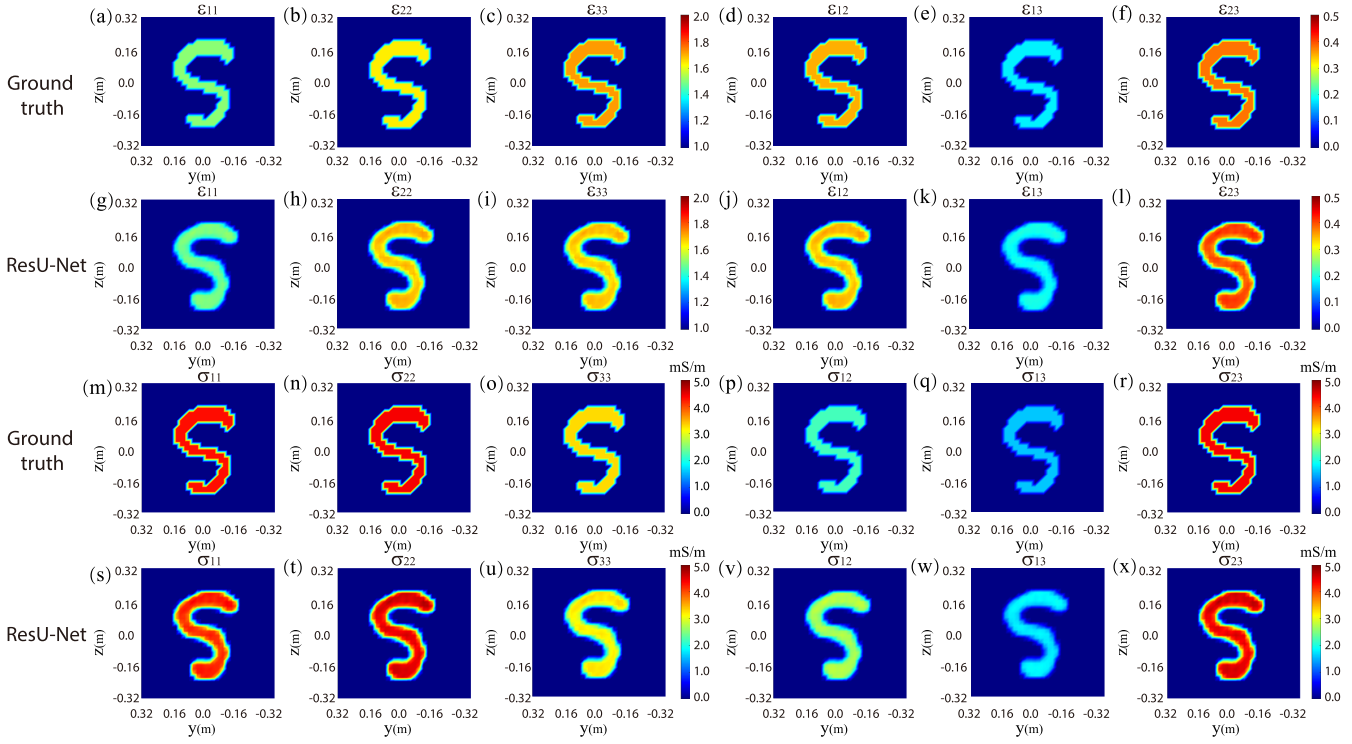

Fig. 7. Test #2: the inversion results of the homogeneous letter "S" by ResU-Net and the ground truths. The first and the third rows display the ground truths of anisotropic permittivity and conductivity. The second and the fourth rows display the reconstructed anisotropic profiles of permittivity and conductivity.

inhomogeneous dielectric parameter distribution. Therefore, we employ the traditional VBIM to further refine the dielectric profiles. Specifically speaking, we compress the FWI computational domain and let it surround the reconstructed shape by ResU-Net. Then, VBIM is implemented in the downsized inversion domain and starts from the model parameters

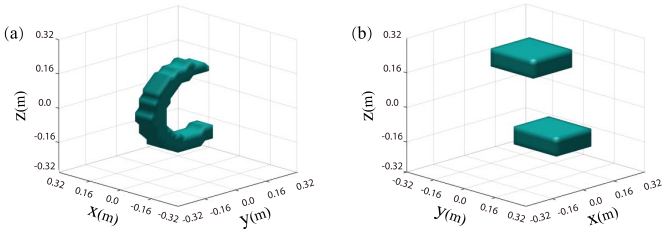

Fig. 8. 3-D shapes of the objects in (a) Test #3 and (b) Test #4.

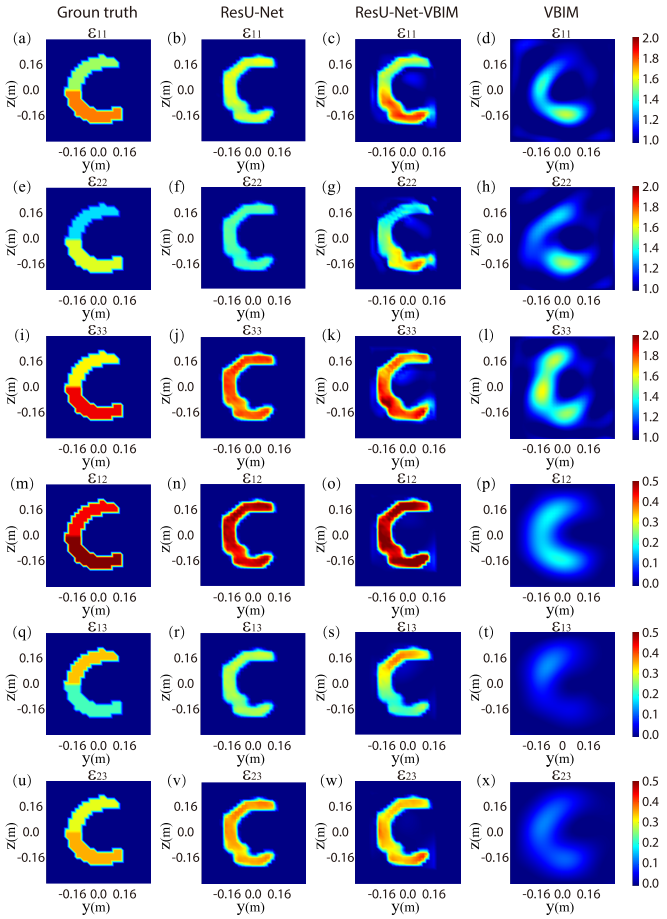

Fig. 9. Test #3: the reconstructed permittivity profiles of the inhomogeneous letter "C" and the ground truths. The first column displays the ground truths. The second column displays the inversion results by ResU-Net. The third column displays the refined inhomogeneous dielectric profiles by VBIM. The fourth column displays the inversion results by pure VBIM.

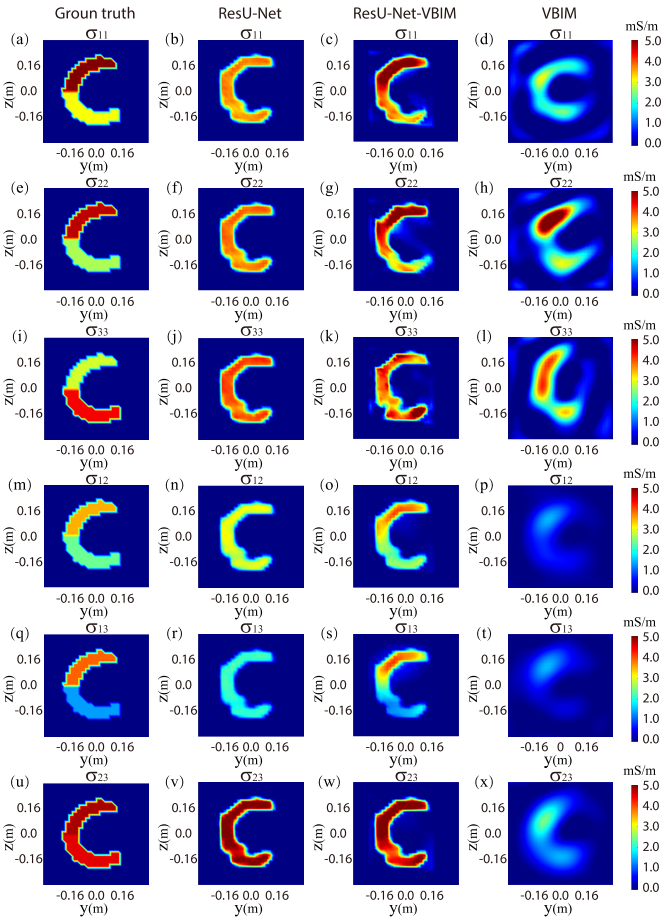

Fig. 10. Test #3: the reconstructed conductivity profiles of the inhomogeneous letter "C" and the ground truths. The first column displays the ground truths. The second column displays the inversion results by ResU-Net. The third column displays the refined inhomogeneous dielectric profiles by VBIM. The fourth column displays the inversion results by pure VBIM.

TABLE III

COMPARISONS OF THE CPU TIME AND MEMORY COST OF RESU-NET-VBIM AND PURE VBIM IN TWO TESTS

Item \ Test	Test #3		Test #4	
	ResU-Net-VBIM	pure VBIM	ResU-Net-VBIM	pure VBIM
CPU time per iteration (min)	7.7	110	17	80
Total memory cost (GB)	21.2	149.9	43.4	149.9

obtained by ResU-Net to reduce the computational cost and increase the inversion accuracy. By comparing the second columns and the third columns in Figs. 9 and 10, we can see that the inhomogeneous dielectric parameter distribution missed by ResU-Net is successfully recovered by VBIM. By comparing the third and fourth columns, we can see that the hybrid method ResU-Net-VBIM has much higher inversion accuracy than the pure VBIM. In addition, the hybrid method also has a lower computational cost than the pure VBIM, which is shown in Fig. 13(a). We can see that the hybrid method and the pure VBIM, respectively, take nine steps and eight steps to converge. The final data misfit of the hybrid method ResU-Net-VBIM becomes less than 0.001 while that of the pure VBIM keeps unchanged when it approaches 0.0077 in the eighth step. However, because the inversion domain of the hybrid method only contains 3933 voxels while that of the pure VBIM contains 32 768 voxels, each iteration of the hybrid method takes around 7.7 min while that of the pure VBIM takes around 110 min. The comparisons of memory cost and CPU time for two methods are given in Table III.

For Test #4, we use two homogeneous cuboids, and the recorded scattered electric fields are contaminated by 30 dB white Gaussian noise, which leads to approximately 3.2%

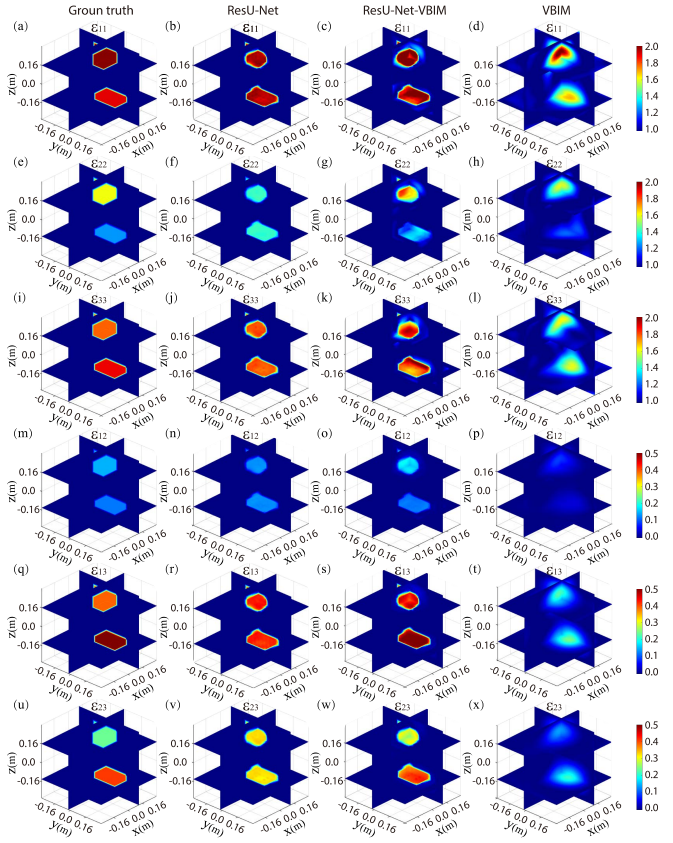

Fig. 11. Test #4: the reconstructed permittivity profiles of two homogeneous cuboids and the ground truths. The first column displays the ground truths. The second column displays the inversion results by ResU-Net. The third column displays the refined dielectric profiles by VBIM. The fourth column displays the inversion results by pure VBIM.

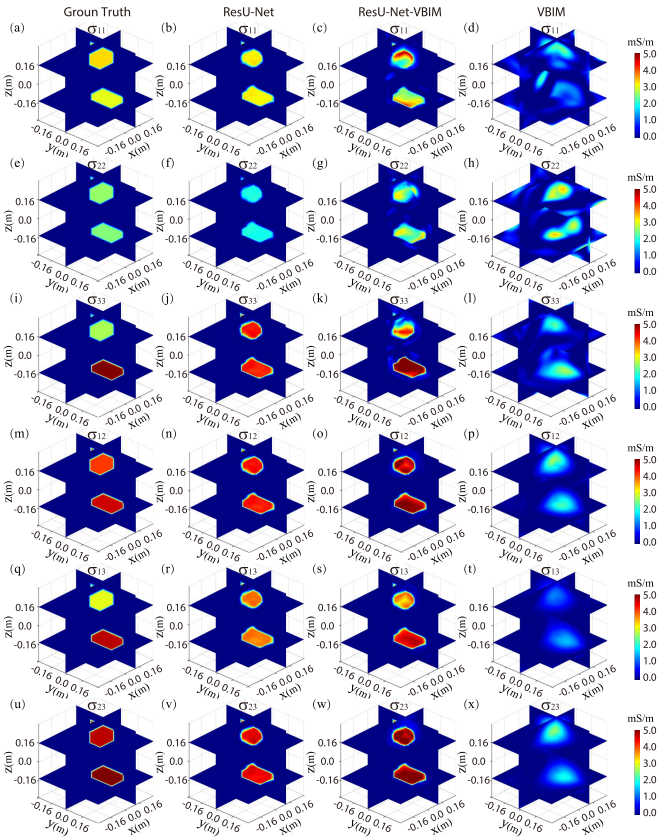

Fig. 12. Test #4: the reconstructed conductivity profiles of two homogeneous cuboids and the ground truths. The first column displays the ground truths. The second column displays the inversion results by ResU-Net. The third column displays the refined dielectric profiles by VBIM. The fourth column displays the inversion results by pure VBIM.

errors of the data. Here, the noise level is defined according to the signal-to-noise ratio (SNR) of power. The purpose of this test is to verify the adaptability of the proposed ResU-Net to noise data and the simultaneous reconstruction of multiple anisotropic objects. As shown in Figs. 11 and 12, the ground truths of the object dielectric profiles and the reconstructed permittivity and conductivity profiles by ResU-Net are displayed in the first and second columns. Obviously, ResU-Net cannot distinguish the different dielectric parameters of two objects although their shapes and locations are effectively reconstructed. Fortunately, the following VBIM solver can compensate for this defect. As shown in the third column of Figs. 11 and 12, not only the difference of the dielectric parameters between two cuboids is recovered by VBIM but also their absolute values are successfully inverted. We also compared the inversion accuracy and the computational cost of the hybrid method of ResU-Net-VBIM with the pure VBIM for the inversion of two cuboids when the field data are contaminated by noise. The inversion results of pure VBIM are shown in the fourth column of Figs. 11 and 12. The comparison of the convergence curves is shown in Fig. 13(b). We can see that the pure VBIM can only invert for the approximate locations of two cuboids. The obtained anisotropic dielectric parameters are far from the ground truths. Meanwhile, the inverted shapes are also severely distorted. The hybrid method

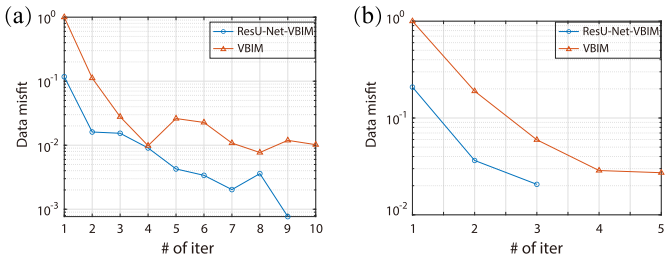

Fig. 13. Convergence curves of VBIM iterations in (a) Test #3 and (b) Test #4.

takes three iterations while the pure VBIM takes four iterations to converge to the noise level. However, because there are only 8526 voxels in the compressed inversion domain of ResU-Net-VBIM, it only costs 50 min to complete the inversion while the pure VBIM costs 400 min. For detailed memory cost and CPU time for two methods, readers can refer to Table III. The above-mentioned inversion results indicate that the trained ResU-Net can only reconstruct homogeneous anisotropic parameter distribution for inhomogeneous objects or multiple homogeneous objects. But the object shapes and locations are correctly obtained. These initial results are fed into the following VBIM solver to reconstruct the inhomogeneous dielectric parameters with a low computational cost.

IV. Conclusion

In this article, a tailored ANN having the overall U-Net framework with its convolutional kernels replaced with residual kernels is proposed to perform the multiparametric FWI of 3-D dielectric arbitrary anisotropic objects. We adopt the residual operation to circumvent gradient vanishing and exploding issues in the deep-learning ANN design and thus account for the nonlinearity and underdetermination of voxel-based 3-D anisotropic inversion. Meanwhile, we also add the SE operations to enhance the prediction accuracy by increasing the information interactions among different channels.

For homogeneous 3-D objects, the trained ResU-Net can simultaneously reconstruct 12 anisotropic parameters with low errors in an instantaneous way, which is shown by Test #1 and Test #2. In other words, the ResU-Net performs effectively in the direct learning mode for the inversion of homogeneous 3-D objects. By contrast, the other two numerical tests in this work indicate that ResU-Net can only accomplish the multiparametric 3-D inhomogeneous anisotropic inversion in the learning-assisted objective-function mode. In other words, ResU-Net only provides the approximate homogeneous 3-D dielectric profiles of the objects in a real-time fashion. The VBIM solver following ResU-Net further improves the inversion accuracy and recovers the inhomogeneity by minimizing the traditional objective function in an iterative way. Test #3 and Test #4 in this work show that compared with the pure VBIM, the hybrid ResU-Net-VBIM can achieve both higher inversion accuracy and lower computational costs. In addition, it also has a certain anti-noise ability.

In the next work, we will try to add some known physics or prior information of EM inverse scattering by anisotropic scatterers into the ANN to reduce the network capacity and training cost. For example, Green's functions in the integral equation are known and it is unnecessary for the ANN to learn it. An independent layer in the ANN can incorporate Green's functions in order to reduce its training cost. Because 12 dielectric parameters share the same scatterer shape, an extra constraint can be added to the 12 channels in the ANN to force the reconstructed model parameters to have the same spatial distribution. Another interesting research topic is to consider the effects of the radiation pattern of real antennas, such as a horn or the Vivaldi, on the inversion results. However, these ideas will be left as future works.

References

[1] A. G. Tijhuis, "Iterative determination of permittivity and conductivity profiles of a dielectric slab in the time domain," *IEEE Trans. Antennas Propag.*, vol. 29, no. 2, pp. 239–245, Mar. 1981.

[2] T. M. Habashy, W. C. Chew, and E. Y. Chow, "Simultaneous reconstruction of permittivity and conductivity profiles in a radially inhomogeneous slab," *Radio Sci.*, vol. 21, no. 4, pp. 635–645, Jul. 1986.

[3] Y. M. Wang and W. C. Chew, "An iterative solution of the two-dimensional electromagnetic inverse scattering problem," *Int. J. Imag. Syst. Technol.*, vol. 1, no. 1, pp. 100–108, Jun. 1989.

[4] W. C. Chew and Y. M. Wang, "Reconstruction of two-dimensional permittivity distribution using the distorted Born iterative method," *IEEE Trans. Med. Imag.*, vol. 9, no. 2, pp. 218–225, Jun. 1990.

[5] N. Zaiping, Y. Feng, Z. Yanwen, and Z. Yerong, "Variational Born iteration method and its applications to hybrid inversion," *IEEE Trans. Geosci. Remote Sens.*, vol. 38, no. 4, pp. 1709–1715, Jul. 2000.

[6] P. M. van den Berg and R. E. Kleinman, "A contrast source inversion method," *Inverse Problems*, vol. 13, no. 6, pp. 1607–1620, Dec. 1997.

[7] L.-P. Song, C. Yu, and Q. H. Liu, "Through-wall imaging (TWI) by radar: 2-D tomographic results and analyses," *IEEE Trans. Geosci. Remote Sens.*, vol. 43, no. 12, pp. 2793–2798, Dec. 2005.

[8] E. Balidemaj *et al.*, "CSI-EPT: A contrast source inversion approach for improved MRI-based electric properties tomography," *IEEE Trans. Med. Imag.*, vol. 34, no. 9, pp. 1788–1796, Sep. 2015.

[9] X. Chen, "Subspace-based optimization method for solving inverse-scattering problems," *IEEE Trans. Geosci. Remote Sens.*, vol. 48, no. 1, pp. 42–49, Aug. 2010.

[10] Y. Liu *et al.*, "A frequency-hopping subspace-based optimization method for reconstruction of 2-D large uniaxial anisotropic scatterers with TE illumination," *IEEE Trans. Geosci. Remote Sens.*, vol. 54, no. 10, pp. 6091–6099, Oct. 2016.

[11] Y. Liu, Z. Zhao, X. Zhu, W. Yang, Z. Nie, and Q.-H. Liu, "A diagonal subspace-based optimization method for reconstruction of 2-D isotropic and uniaxial anisotropic dielectric objects," *IEEE Geosci. Remote Sens. Lett.*, vol. 14, no. 8, pp. 1318–1322, Aug. 2017.

[12] X. Ye *et al.*, "Application of subspace-based distorted-Born iteration method in imaging biaxial anisotropic scatterer," *IEEE Trans. Comput. Imag.*, vol. 6, pp. 1486–1492, 2020.

[13] Z. Nie and Y. Zhang, "Hybrid Born iterative method in low-frequency inverse scattering problem," *IEEE Trans. Geosci. Remote Sens.*, vol. 36, no. 3, pp. 749–753, May 1998.

[14] F. Li, Q. H. Liu, and L.-P. Song, "Three-dimensional reconstruction of objects buried in layered media using Born and distorted Born iterative methods," *IEEE Geosci. Remote Sens. Lett.*, vol. 1, no. 2, pp. 107–111, Apr. 2004.

[15] C. Yu *et al.*, "Active microwave imaging II: 3-D system prototype and image reconstruction from experimental data," *IEEE Trans. Microw. Theory Techn.*, vol. 56, no. 4, pp. 991–1000, Apr. 2008.

[16] W. Zhang and Q. H. Liu, "Three-dimensional scattering and inverse scattering from objects with simultaneous permittivity and permeability contrasts," *IEEE Trans. Geosci. Remote Sens.*, vol. 53, no. 1, pp. 429–439, Jan. 2015.

[17] J. Zhuo, L. Ye, F. Han, L. Xiong, and Q. H. Liu, "Multiparametric electromagnetic inversion of 3-D biaxial anisotropic objects embedded in layered uniaxial media using VBIM enhanced by structural consistency constraint," *IEEE Trans. Antennas Propag.*, vol. 68, no. 6, pp. 4774–4785, Jun. 2020.

[18] J. Wang, J. Li, Y. Chen, F. Han, and Q. H. Liu, "Simulation of 3-D electromagnetic scattering and inverse scattering by arbitrary anisotropic dielectric objects embedded in layered arbitrary anisotropic media," *IEEE Trans. Antennas Propag.*, vol. 68, no. 8, pp. 6473–6478, Aug. 2020.

[19] J. Li, J. Zhuo, Z. Guan, F. Han, and Q. H. Liu, "3-D electromagnetic scattering and inverse scattering by magnetodielectric objects with arbitrary anisotropy in layered uniaxial media," *IEEE Trans. Antennas Propag.*, vol. 68, no. 2, pp. 1009–1022, Feb. 2020.

[20] L. E. Sun, "Parametric inversion of 3-D anisotropic permittivities from scattered electromagnetic fields," *IEEE Trans. Antennas Propag.*, vol. 66, no. 6, pp. 3027–3033, Jun. 2018.

[21] C. Qiu *et al.*, "Multifrequency 3-D inversion of GREATEM data by BCGS-FFT-BIM," *IEEE Trans. Geosci. Remote Sens.*, vol. 57, no. 4, pp. 2439–2448, Apr. 2019.

[22] C. Qiu, B. Liang, F. Han, J. Li, G. Fang, and Q. H. Liu, "3-D full-wave inversion of helicopter transient electromagnetic data in frequency domain," *IEEE Trans. Geosci. Remote Sens.*, vol. 58, no. 7, pp. 4928–4938, Jul. 2020.

[23] R. Hong *et al.*, "3-D MRI-based electrical properties tomography using the volume integral equation method," *IEEE Trans. Microw. Theory Techn.*, vol. 65, no. 12, pp. 4802–4811, Dec. 2017.

[24] A. Afsari, A. M. Abbosh, and Y. Rahmat-Samii, "Modified Born iterative method in medical electromagnetic tomography using magnetic field fluctuation contrast source operator," *IEEE Trans. Microw. Theory Techn.*, vol. 67, no. 1, pp. 454–463, Jan. 2019.

[25] M. Ambrosanio, P. Kosmas, and V. Pascazio, "A multithreshold iterative DBIM-based algorithm for the imaging of heterogeneous breast tissues," *IEEE Trans. Biomed. Eng.*, vol. 66, no. 2, pp. 509–520, Feb. 2019.

[26] L.-P. Song, Q. H. Liu, F. Li, and Z. Q. Zhang, "Reconstruction of three-dimensional objects in layered media: Numerical experiments," *IEEE Trans. Antennas Propag.*, vol. 53, no. 4, pp. 1556–1561, Apr. 2005.

[27] Z. Q. Zhang and Q. H. Liu, "Three-dimensional nonlinear image reconstruction for microwave biomedical imaging," *IEEE Trans. Biomed. Eng.*, vol. 51, no. 3, pp. 544–548, Mar. 2004.

[28] P. Zhao *et al.*, "An improved subspace-regularized DBIM-MLGFIM method for three-dimensional inverse scattering problems," *IEEE Trans. Antennas Propag.*, vol. 69, no. 5, pp. 2798–2809, May 2021.
[29] Y. Chen, J. Li, J. Zhuo, F. Han, and Q. H. Liu, "Fast multiparametric electromagnetic full-wave inversion via solving contracting scattering data equations optimized by the 3-D MRF model," *IEEE Trans. Microw. Theory Techn.*, vol. 68, no. 11, pp. 4515–4527, Nov. 2020.
[30] S. Caorsi and P. Gamba, "Electromagnetic detection of dielectric cylinders by a neural network approach," *IEEE Trans. Geosci. Remote Sens.*, vol. 37, no. 2, pp. 820–827, Mar. 1999.
[31] I. T. Rekanos, "Neural-network-based inverse-scattering technique for online microwave medical imaging," *IEEE Trans. Magn.*, vol. 38, no. 2, pp. 1061–1064, Mar. 2002.
[32] X. Chen, Z. Wei, M. Li, and P. Rocca, "A review of deep learning approaches for inverse scattering problems," *Prog. Electromagn. Res.*, vol. 167, pp. 67–81, 2020.
[33] Z. Wei and X. Chen, "Deep-learning schemes for full-wave nonlinear inverse scattering problems," *IEEE Trans. Geosci. Remote Sens.*, vol. 57, no. 4, pp. 1849–1860, Apr. 2019.
[34] H. M. Yao, W. E. I. Sha, and L. Jiang, "Two-step enhanced deep learning approach for electromagnetic inverse scattering problems," *IEEE Antennas Wireless Propag. Lett.*, vol. 18, no. 11, pp. 2254–2258, Nov. 2019.
[35] L.-Y. Xiao, J. Li, F. Han, W. Shao, and Q. H. Liu, "Dual-module NMM-IEM machine learning for fast electromagnetic inversion of inhomogeneous scatterers with high contrasts and large electrical dimensions," *IEEE Trans. Antennas Propag.*, vol. 68, no. 8, pp. 6245–6255, Aug. 2020.
[36] L. Li, L. G. Wang, F. L. Teixeira, C. Liu, A. Nehorai, and T. J. Cui, "DeepNIS: Deep neural network for nonlinear electromagnetic inverse scattering," *IEEE Trans. Antennas Propag.*, vol. 67, no. 3, pp. 1819–1828, Mar. 2019.
[37] L. Zhang, K. Xu, R. Song, X. Ye, G. Wang, and X. Chen, "Learning-based quantitative microwave imaging with a hybrid input scheme," *IEEE Sensors J.*, vol. 20, no. 24, pp. 15007–15013, Dec. 2020.
[38] X. Ye, Y. Bai, R. Song, K. Xu, and J. An, "An inhomogeneous background imaging method based on generative adversarial network," *IEEE Trans. Microw. Theory Techn.*, vol. 68, no. 11, pp. 4684–4693, Nov. 2020.
[39] Y. Huang, R. Song, K. Xu, X. Ye, C. Li, and X. Chen, "Deep learning-based inverse scattering with structural similarity loss functions," *IEEE Sensors J.*, vol. 21, no. 4, pp. 4900–4907, Feb. 2021.
[40] Y. Sanghvi, Y. Kalepu, and U. Khankhoje, "Embedding deep learning in inverse scattering problems," *IEEE Trans. Comput. Imag.*, vol. 6, pp. 46–56, 2020.
[41] G. Chen, P. Shah, J. Stang, and M. Moghaddam, "Learning-assisted multimodality dielectric imaging," *IEEE Trans. Antennas Propag.*, vol. 68, no. 3, pp. 2356–2369, Mar. 2020.
[42] Y. Chen, L.-Y. Xiao, J. Zhuo, F. Han, and Q. H. Liu, "Quantitative electromagnetic inversion of irregular scatterers based on a threefold hybrid method," *IEEE Trans. Antennas Propag.*, vol. 69, no. 12, pp. 8664–8674, Dec. 2021.
[43] Z. Wei and X. Chen, "Physics-inspired convolutional neural network for solving full-wave inverse scattering problems," *IEEE Trans. Antennas Propag.*, vol. 67, no. 9, pp. 6138–6148, Sep. 2019.
[44] J. Xiao, J. Li, Y. Chen, F. Han, and Q. H. Liu, "Fast electromagnetic inversion of inhomogeneous scatterers embedded in layered media by Born approximation and 3-D U-Net," *IEEE Geosci. Remote Sens. Lett.*, vol. 17, no. 10, pp. 1677–1681, Oct. 2020.
[45] L.-Y. Xiao, J. Li, F. Han, H.-J. Hu, M. Zhuang, and Q. H. Liu, "Super-resolution 3-D microwave imaging of objects with high contrasts by a semijoin extreme learning machine," *IEEE Trans. Microw. Theory Techn.*, vol. 69, no. 11, pp. 4840–4855, Nov. 2021.
[46] O. Ronneberger, P. Fischer, and T. Brox, "U-Net: Convolutional networks for biomedical image segmentation," in *Proc. Int. Conf. Med. Image Comput. Comput.-Assist. Intervent.*, 2015, pp. 234–241.
[47] K. He, X. Zhang, S. Ren, and J. Sun, "Deep residual learning for image recognition," in *Proc. IEEE Conf. Comput. Vis. Pattern Recognit. (CVPR)*, Jun. 2016, pp. 770–778.
[48] J. Hu, L. Shen, S. Albanie, G. Sun, and E. Wu, "Squeeze-and-excitation networks," *IEEE Trans. Pattern Anal. Mach. Intell.*, vol. 42, no. 8, pp. 2011–2023, Apr. 2020.
[49] W. C. Chew, *Waves Fields Inhomogeneous Media*. New York, NY, USA: IEEE Press, 1995, ch. 7.
[50] G. L. Wang, T. Barber, P. Wu, D. Allen, and A. Abubakar, "Fast inversion of triaxial induction data in dipping crossbedded formations," *Geophysics*, vol. 82, no. 2, pp. D31–D45, Mar. 2017.
[51] K. He, X. Zhang, S. Ren, and J. Sun, "Identity mappings in deep residual networks," 2016, *arXiv:1603.05027*.
[52] S.-W. Fu, T.-W. Wang, Y. Tsao, X. Lu, and H. Kawai, "End-to-end waveform utterance enhancement for direct evaluation metrics optimization by fully convolutional neural networks," *IEEE/ACM Trans. Audio, Speech, Language Process.*, vol. 26, no. 9, pp. 1570–1584, Sep. 2018.
[53] D. P. Kingma and J. Ba, "Adam: A method for stochastic optimization," 2014, *arXiv:1412.6980*.
[54] T. Lan, N. Liu, F. Han, and Q. H. Liu, "Joint petrophysical and structural inversion of electromagnetic and seismic data based on volume integral equation method," *IEEE Trans. Geosci. Remote Sens.*, vol. 57, no. 4, pp. 2075–2086, Apr. 2019.
[55] Y. LeCun, L. Bottou, Y. Bengio, and P. Haffner, "Gradient-based learning applied to document recognition," *Proc. IEEE*, vol. 86, no. 11, pp. 2278–2324, Nov. 1998.

Junjie Fei received the B.S. degree in communication engineering from Chongqing University, Chongqing, China, in 2020. He is currently pursuing the master's degree with Xiamen University, Xiamen, China.

His research interest is artificial intelligence, machine learning, and applying these techniques to electromagnetic inverse scattering and imaging problems.

Yanjin Chen received the B.S. degree in mechanical and electronic engineering from Hainan University, Hainan, China, in 2017, and the M.S. degree in the electromagnetic field and wireless technology from Xiamen University, Xiamen, China, in 2021.

He is currently a Research Assistant with the Fujian Provincial Key Laboratory of Electromagnetic Wave Science and Detection Technology, Xiamen University. His research interest includes applying machine learning techniques to electromagnetic inverse scattering problems.

Miao Zhong received the B.S. degree in communication engineering from Nanchang Hangkong University, Nanchang, China, in 2020. She is currently pursuing the master's degree with Xiamen University, Xiamen, China.

Her research interests include electromagnetic inverse scattering and full-wave inversion.

Feng Han (Senior Member, IEEE) received the B.S. degree in electronic science from Beijing Normal University, Beijing, China, in 2003, the M.S. degree in geophysics from Peking University, Beijing, in 2006, and the Ph.D. degree in electrical engineering from Duke University, Durham, NC, USA, in 2011.

Since 2015, he has been with Xiamen University, Xiamen, China, where he is currently an Associate Professor of the Institute of Electromagnetics and Acoustics. He has authored or coauthored over 50 articles in refereed journals. His research interests include electromagnetic scattering and inverse scattering in complex media, fast full-wave electromagnetic inversion based on machine learning, configuration of the antenna array for electromagnetic inverse problems, and geophysical electromagnetic exploration and inversion.